Signatures of Structural Disorder in the Developing *Drosophila* Germband Epithelium

Christian Cupo,[1] Cole Allan,[1,2] Vikram Ailiani,[1] and Karen E. Kasza[1,*]
[1]*Department of Mechanical Engineering, Columbia University, New York, New York 10027, USA*
[2]*Department of Mechanical Engineering, Stanford University, Stanford, California 94305, USA*

(Received 27 February 2024; accepted 1 October 2024; published 21 October 2024)

Epithelial cells generate functional tissues in developing embryos through collective movements and shape changes. In some morphogenetic events, a tissue dramatically reorganizes its internal structure—often generating high degrees of structural disorder—to accomplish changes in tissue shape. However, the origins of structural disorder in epithelia and what roles it might play in morphogenesis are poorly understood. We study this question in the *Drosophila* germband epithelium, which undergoes dramatic changes in internal structure as cell rearrangements drive elongation of the embryo body axis. Using two order parameters that quantify volumetric and shear disorder, we show that structural disorder increases during body axis elongation and is strongly linked with specific developmental processes. Both disorder metrics begin to increase around the onset of axis elongation, but then plateau at values that are maintained throughout the process. Notably, the disorder plateau values for volumetric disorder are similar to those for random cell packings, suggesting this may reflect a limit on tissue behavior. In mutant embryos with disrupted external stresses from the ventral furrow, both disorder metrics reach wild-type maximum disorder values with a delay, correlating with delays in cell rearrangements. In contrast, in mutants with disrupted internal stresses and cell rearrangements, volumetric disorder is reduced compared to wild type, and shear disorder depends on specific external stress patterns. Together, these findings demonstrate that internal and external stresses both contribute to epithelial tissue disorder and suggest that the maximum values of disorder in a developing tissue reflect physical or biological limits on morphogenesis.

DOI: 10.1103/PRXLife.2.043004

I. INTRODUCTION

Epithelial tissue sheets comprise confluent packings of cells that undergo dramatic changes in overall shape and internal structure during development. The shapes and packings of cells in embryonic epithelia are diverse and can be regular and ordered or highly irregular and disordered. Moreover, the cell packings of a single tissue can change dramatically during development, mediated by changes in cell shapes and movements within the tissue [1–3]. For example, cells in the *Drosophila* germband epithelium initially tend to take on roughly regular, hexagonal shapes [4], which are optimized tilings for the densest arrangement of cells [5], but become more irregular as the tissue remodels during body axis elongation [4]. However, it is not well understood what biological factors regulate tissue disorder or how tissue disorder might influence tissue behavior and function.

Convergent extension of the *Drosophila* germband epithelium during body axis elongation is a powerful model for studying the biological and physical factors that regulate epithelial structure and remodeling [6–13]. Internal stresses from planar polarized actomyosin contractility and external stresses from neighboring developmental events both contribute to rapid elongation of the germband along the anterior-posterior (AP) axis of the embryo [7–12,14–18]. This global tissue elongation is mediated by oriented cell rearrangements and cell shape changes that allow the tissue to remodel and flow [8,10,13–15,19,20]. Although it has been observed that cell shapes change and become more disordered during axis elongation [4,13], the mechanisms driving this disorder and the resulting impacts on tissue elongation remain poorly understood.

The cell rearrangements and cell shape changes that mediate tissue remodeling are thought to be driven by an interplay between local, internal stresses and global, embryo-scale stresses. Internal stresses are generated by a planar polarized pattern of actomyosin contractility that is thought to arise from AP patterning systems [6,7,21] along with mechanosensitive feedback mechanisms [9,18]. In addition, the germband experiences external stresses from ventral furrow formation (VFF) pulling along the dorsal-ventral (DV) axis and posterior midgut invagination (PMI) pulling along the AP axis [10–12,15,16,20,22,23]. A recent study has proposed that the stretch from the ventral furrow provides a mechanical cue to enrich myosin planar polarity and facilitate germband extension [18]. Together, these internal and external stresses are thought to control tissue structure and remodeling, but it has been difficult to decouple the effects of each.

Tissue structure is likely to influence biological and mechanical behaviors of the tissue. Work from our group and others has shown that the *average* cell shape in a tissue is a good predictor of whether the tissue will remodel and flow,

*Contact author: karen.kasza@columbia.edu

similar to a fluid, or instead resist remodeling, similar to an elastic solid [13,24–28]. Recent studies have demonstrated links between metrics for the *heterogeneity* in local tissue structure, i.e., structural disorder, and transitions in solidlike, liquidlike, and gaslike behavior of cultured tissues and developing embryos [29]. However, it remains unclear if and how structural order or disorder in a tissue might facilitate tissue remodeling.

Here, we study structural disorder in the developing *Drosophila* germband epithelium by analyzing volumetric and shear order parameters. We show that structural disorder in the germband increases during axis elongation in characteristic steps that coincide with developmental events in the embryo. We uncover that internal and external stress patterns contribute in distinct ways to volumetric and shear disorder, which are in turn linked with the rates and final extents of tissue remodeling. We find that the maximum magnitudes of structural disorder in the germband are in the range expected for purely random cell packings that have minimum cell-cell spacings, suggesting geometrical constraints on tissue disorder in this context. Overall, this work uncovers the biological and physical mechanisms that contribute to epithelial tissue disorder and highlight a central role for tissue disorder in epithelial remodeling and morphogenesis.

II. RESULTS

A. Structural disorder increases in the germband epithelium during body axis elongation

To explore how structural disorder evolves in developing epithelial tissues, we analyzed volumetric and shear disorder in the developing *Drosophila* embryo during body axis elongation. In *Drosophila*, the embryonic body axis rapidly doubles in length along the anterior-posterior (AP) axis through convergent extension movements of the germband epithelium [Fig. 1(a)] [6]. Tissue elongation is mediated in large part by rapid rearrangements of epithelial cells within the germband [Fig. 1(b)] [8,19]. To analyze epithelial tissue structure, we fluorescently labeled cell membranes, imaged the embryo by confocal microscopy, segmented the time-lapse movies, and triangulated the centroids of cells within the ventrolateral region of the germband [Fig. 1(c)] (see Materials and Methods).

To explore tissue structural disorder, we quantified the local volume and shear deformations in the triangulated tissue, as previously described [29]. Briefly, for the nth triangle in the tissue triangulation, the volume and shear invariants, vol_{n} and $shear_{\mathrm{n}}$, are calculated by comparing a deformed state to a reference state and determining the deformation [Fig. 1(d)]. vol_{n} reflects how the triangle area deviates from the average area at each time point [Fig. 1(e)], and $shear_{\mathrm{n}}$ reflects the distortion from an equilateral triangle of the same area [Fig. 1(f)]. Both invariants would be minimized if the triangulation comprises equilateral triangles of uniform area, i.e., a regular, isotropic honeycomb lattice has no volumetric or shear disorder. Triangles with small values of vol_{n} have areas close to the average area of all the triangles analyzed at that time point, while triangles with much larger or smaller areas than the average have large positive or negative values of vol_{n}, respectively. Triangles with small values of $shear_{\mathrm{n}}$ have geometries similar to an equilateral triangle, while triangles with large values of $shear_{\mathrm{n}}$ display strong distortions relative to an equilateral triangle. We find that the variation across the germband of vol_{n} [Fig. 1(g)] and $shear_{\mathrm{n}}$ [Fig. 1(h)] tends to increase over time during axis elongation (see also Fig. S1 of the Supplemental Material [30]).

To quantify the growing structural disorder, we calculated two structural order parameters, Φ_{vol} and Φ_{shear} (Materials and Methods) [29]. The volumetric order parameter, $\Phi_{\mathrm{vol}} = \langle[\ln(vol_n)]^2\rangle$, represents density fluctuations across the tissue. The shear order parameter, $\Phi_{\mathrm{shear}} = \langle\ln(shear_n)\rangle$, represents the irregularity of triangles and will be nonzero for configurations in which triangles deviate from equilateral triangles, both due to the variability between triangles and any overall stretch in the tissue. Prior to axis elongation, both order parameters take on small, relatively constant values [Figs. 2(a)–2(c)], indicating low levels of structural disorder in the germband. Around the onset of axis elongation, Φ_{vol} and Φ_{shear} both begin to increase [Figs. 2(a)–2(c)], indicating growing structural disorder associated with tissue elongation. The values of Φ_{vol} and Φ_{shear} are not strongly affected by the specific choice of analysis region (Figs. S2 and S3 [30]) or embryo mounting procedure (Fig. S4 [30]). Moreover, the overall trends are not strongly affected by the tissue triangulation method used (Fig. S5 [30]). Of note, the qualitative trends in Φ_{vol} are independent of whether disorder is measured for the tissue triangulation or for the cell areas themselves (Fig. S5 [30]).

We find that Φ_{vol} and Φ_{shear} increase in characteristic patterns that are consistent among wild-type embryos [Figs. 2(a)–2(c)]. We identified patterns in the growing disorder by finding points in the disorder versus time curves where there are abrupt changes in slope. The first increase in disorder is an increase in Φ_{shear} 3–4 min before the onset of axis elongation, which occurs in the absence of changes in Φ_{vol} [Figs. 2(a)–2(c)]. Notably, this increase in germband shear disorder occurs just after the neighboring ventral furrow forms [Fig. 2(d)] and has its own increase in Φ_{shear} [Fig. 2(e) and Fig. S6 [30]], suggesting that shear disorder in the germband is influenced by external stresses from the ventral furrow stretching the germband.

Just after the onset of axis elongation, which begins at $t = 0$ min, volumetric disorder begins to increase. The increase in Φ_{vol} aligns with the start of cell rearrangements [Fig. 2(f)], in which cells change contacts with their neighbors to promote tissue remodeling. These rearrangement events are driven by internal stresses from planar polarized actomyosin, suggesting that cell shape changes associated with rearrangement events contribute to volumetric disorder. Around the same time, Φ_{shear} temporarily plateaus, corresponding to tissue-scale reorientation of cell shapes from being stretched along the DV axis to being stretched along the AP axis (Fig. S7 [30]), likely due to competing effects of the ventral furrow pulling along the DV axis and the posterior midgut pulling along the AP axis.

Notably, we find that both Φ_{vol} and Φ_{shear} plateau at $t = 5$–10 min at maximum values that are then maintained throughout the rest of the process. Φ_{vol} reaches a maximum 5 min after the onset of axis elongation, which corresponds to the timing of the maximum rate of cell rearrangement in the germband [Fig. 2(f)]. Φ_{shear} plateaus a few minutes

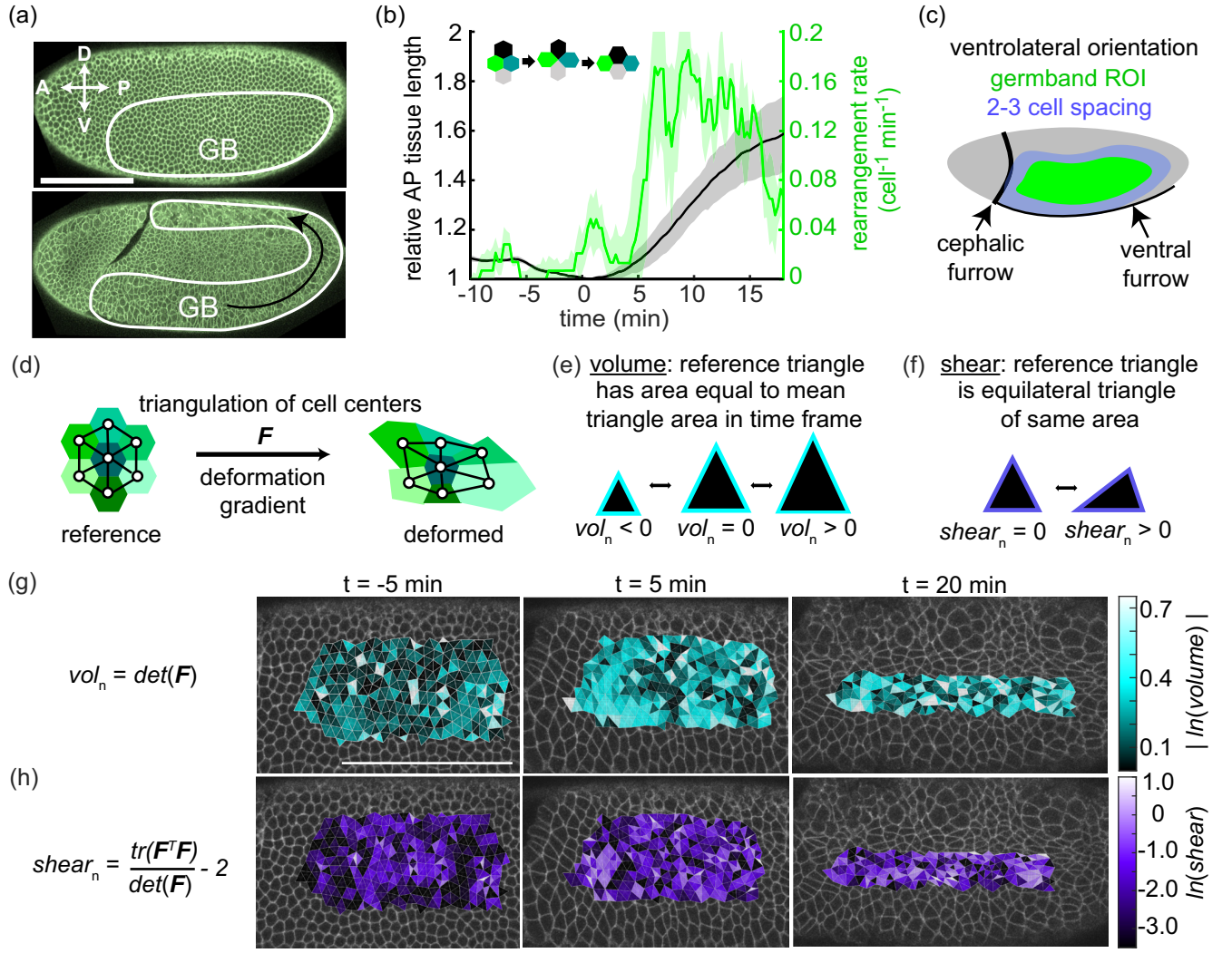

FIG. 1. Structural disorder in the germband epithelium of the developing *Drosophila* embryo. (a) During body axis elongation, the germband epithelium (GB) undergoes convergent extension, narrowing along the dorsal-ventral (DV) axis and extending to twice its length along the anterior-posterior (AP) axis. (b) Tissue elongation (black) is facilitated by cellular rearrangements (green) that drive internal structural remodeling. The mean and standard deviation between four embryos is plotted. (c) Embryos are imaged in a ventrolateral orientation, and an ROI for analyses is selected such that it is two to three cells away from the cephalic and ventral furrows. (d) Structural disorder in the tissue can be characterized by triangulating cell centroids and comparing to a reference configuration. (e) Volumetric disorder: each triangle is compared to a reference triangle with an area equal to the average triangle area at that time point. (f) Shear disorder: each triangle is compared to a reference triangle that is an equilateral triangle of equal area. (g), (h) Triangulation of the germband at $t = -5,\ 5$, and 20 min. The color of each triangle represents its volumetric (density variation) or shear (irregularity compared to an equilateral triangle) deformation. Scale bar, 100 μm.

later. These disorder plateaus begin well before the end of axis elongation, while the tissue is still rapidly remodeling, suggesting that the maximum disorder plateaus might reflect a biological or physical constraint in the germband.

Taken together, these results demonstrate that structural disorder increases in the germband around the onset of axis elongation before reaching maximum plateau values that are then maintained through the rest of the process. Before reaching these plateaus, structural disorder increases in characteristic patterns or signatures, which are correlated with developmental events in the embryo.

B. External stresses from the ventral furrow influence germband structural disorder but not the maximum disorder reached

The timing of the initial increase in Φ_{shear} suggests a link between structural disorder in the germband and stresses from furrow formation in the neighboring ventral region of the embryo. To test this directly, we studied tissue disorder in *snail twist* (*sna twi*) mutant embryos in which ventral furrow formation (VFF) is disrupted [Fig. 3(d)]. Initially, the germband of *sna twi* embryos displays lower values of Φ_{vol} and Φ_{shear} compared to wild-type embryos [Figs. 3(a)–3(c) and Fig. S8 [30]], indicating more ordered tissue structure. The initial

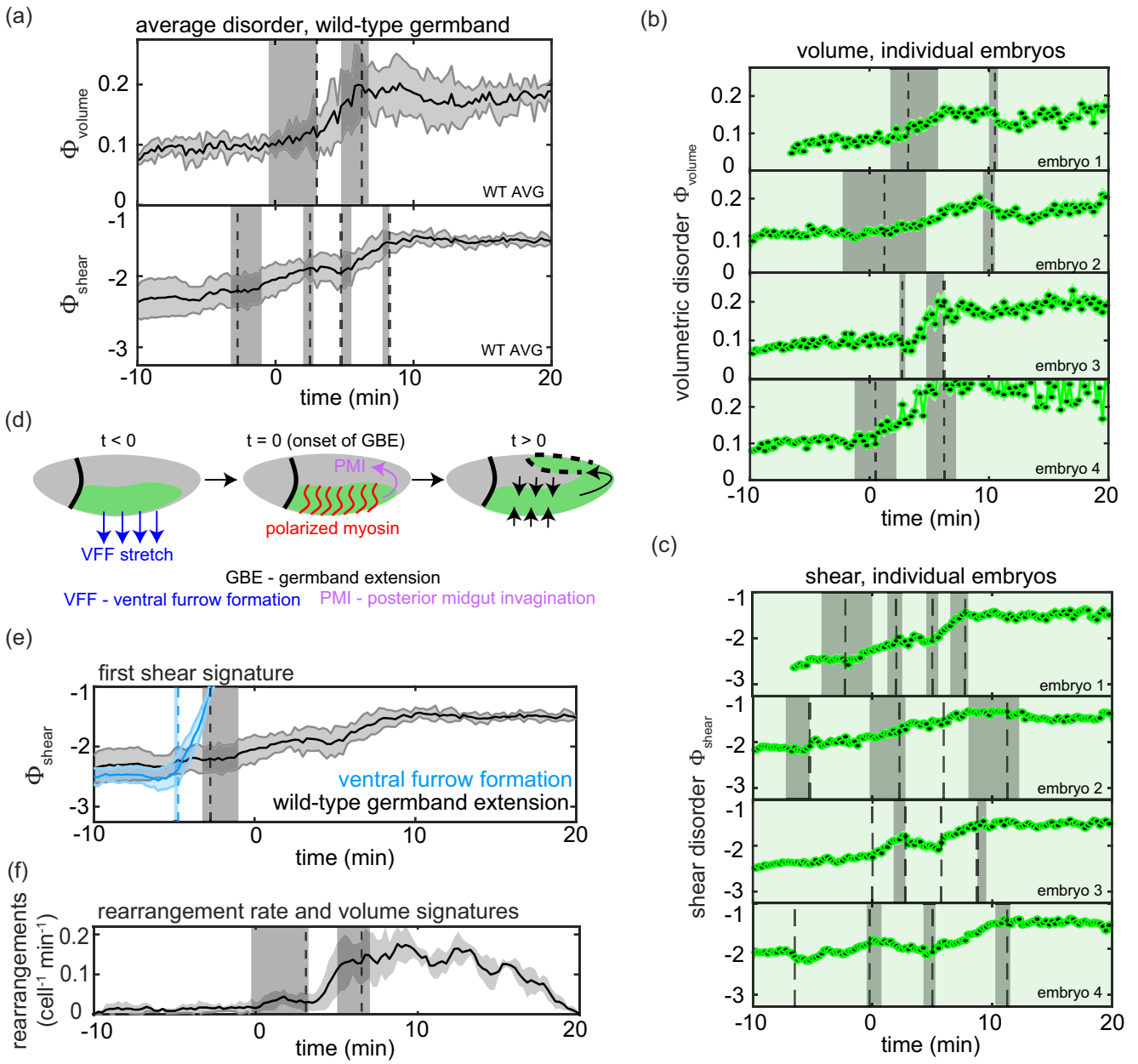

FIG. 2. Structural disorder grows in the germband epithelium during axis elongation. (a) The volumetric order parameter Φ_{vol} and shear order parameter Φ_{shear} averaged across embryos ($N = 4$ embryos). Shaded error bars represent standard deviation. Vertical dashed lines represent time points at which abrupt slope changes occur. The positions of the n changes in slope are identified using $n + 1$ linear fits and minimizing the residuals. Vertical shaded regions around these lines represent values where the root-mean-squared deviation is within 10%. (b), (c) Individual Φ_{vol} and Φ_{shear} curves over time for four wild-type embryos. Characteristic patterns or signatures of disorder are shared among embryos. (d) Schematics of axis elongation highlighting key developmental events in the germband (green) and neighboring regions of the embryo. (e) The first increase of Φ_{shear} in the germband (black) immediately follows an increase of Φ_{shear} in the neighboring ventral furrow region (blue). (f) The initial increase and final plateau in Φ_{vol} align with the onset of cell rearrangement events and the time point of maximum rearrangement rate, respectively.

increase in Φ_{shear} observed around $t = -3$ min in wild-type embryos is not present in *sna twi* embryos, demonstrating that this increase in shear disorder is driven by the ventral furrow. Instead, in *sna twi* embryos, Φ_{shear} and Φ_{vol} begin to increase just after $t = 0$ min.

Despite starting out more ordered, Φ_{shear} and Φ_{vol} in the germband of *sna twi* embryos reach the same maximum plateau values as in wild-type embryos, but with a time delay [Fig. 3(a)]. Once they begin to increase, the rates of disorder growth are comparable in *sna twi* and wild-type embryos [Figs. 3(f) and 3(g)], resulting in time delays of 3.25 min for Φ_{vol} and 6 min for Φ_{shear} for reaching the plateau values [Fig. 3(a)]. *sna twi* embryos also display a delay in cell rearrangements, reaching the same maximum rearrangement rate as wild-type embryos but with an $\sim$3 min delay [Fig. 3(e)]. These delays in *sna twi* embryos

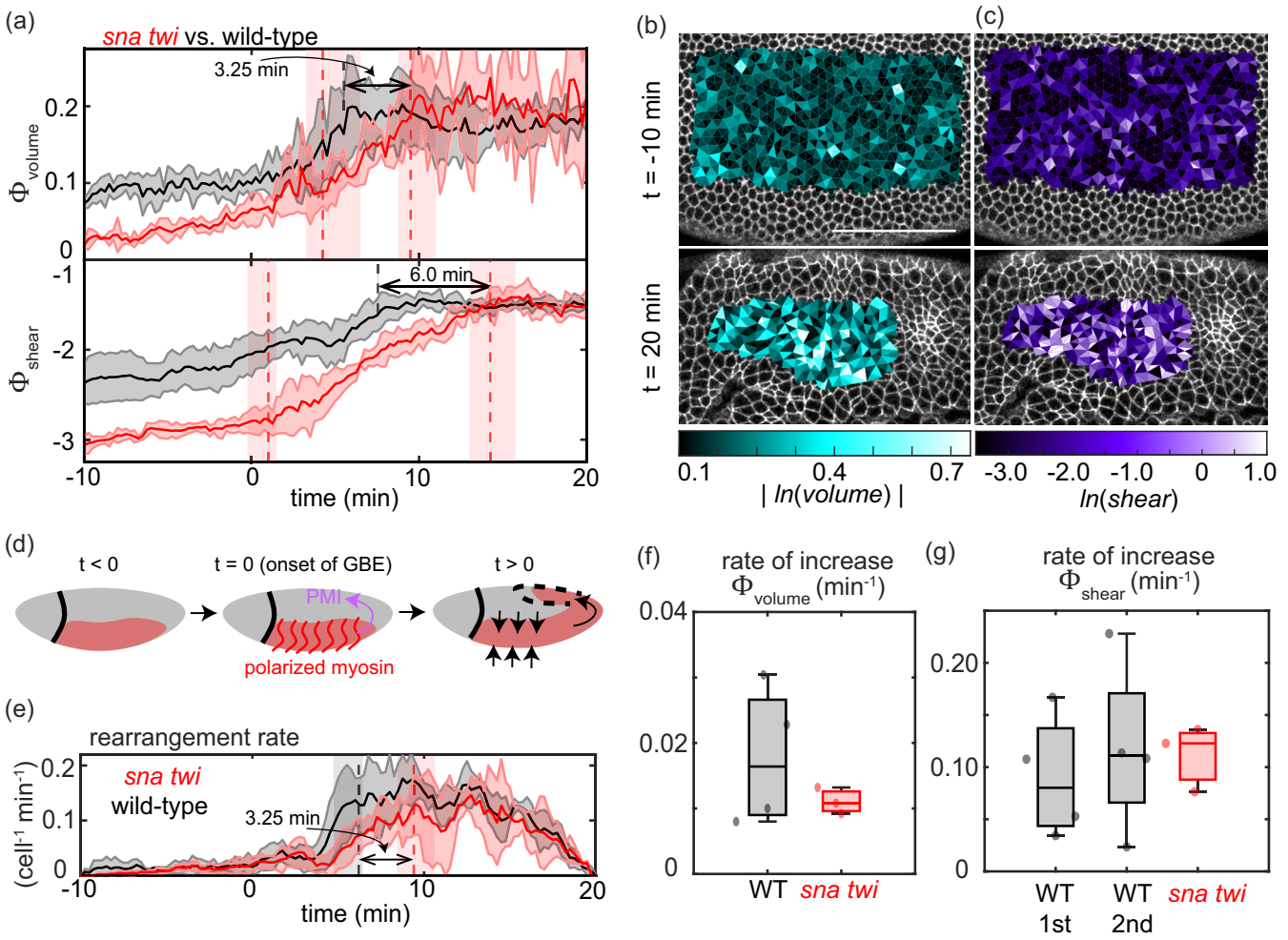

FIG. 3. Structural disorder growth in the germband epithelium is delayed by disruption of ventral furrow invagination in *sna twi* mutant embryos. (a) Average Φ_{vol} and Φ_{shear} in the germband of *sna twi* mutant embryos ($N = 3$) (red) compared to wild type ($N = 4$) (black). Shaded error bars represent standard deviation between embryos. Vertical red dashed lines indicate positions of slope changes in curves from *sna twi* embryos. For reference, dashed, vertical black lines represent the timing of slope changes at the maximum disorder plateau in wild-type embryos. The maximum plateau values of Φ_{vol} and Φ_{shear} are delayed by 3.25 and 6 min, respectively, compared to wild-type embryos. (b), (c) Volumetric (cyan) and shear (purple) deformation for the tissue triangulation at $t = -10$ and 20 min. (d) Schematics of key developmental events in *sna twi* mutant embryos with disrupted ventral furrow invagination. Disrupting the ventral furrow alters the external stress patterns acting on the germband. (e) Cell rearrangement rate in *sna twi* (red) and wild-type (black) embryos. Vertical dashed lines represent the slope change signature in Φ_{vol} that marks the time point of reaching the maximum Φ_{vol} in *sna twi* (red) and wild-type (black) embryos [cf. panel (a)]. In *sna twi* embryos, the delay in reaching maximum Φ_{vol} aligns with a delay in reaching the maximum rearrangement rate. (f) Rate of volumetric disorder growth [average slope of $\Phi_{vol}(t)$ between slope changes] in wild-type and *sna twi* embryos. (g) Rate of shear disorder growth [average slope of $\Phi_{shear}(t)$ between slope changes] in wild-type and *sna twi* embryos. WT 1st and WT 2nd correspond to the first and second shear disorder increases in Fig. 2(a).

suggest that the ventral furrow might facilitate rapid axis elongation in wild-type embryos, an idea consistent with recent reports [18].

Notably, the maximum plateau values of Φ_{shear} and Φ_{vol} are the same in *sna twi* and wild-type embryos, indicating that external stresses from the ventral furrow do not affect the final structural disorder in the germband. One possible explanation is that loss of external stresses from the ventral furrow could be compensated for by other mechanisms. Alternatively, it is possible that the ventral furrow only influences germband tissue disorder during the first minutes of axis elongation before other factors dominate, such as internal myosin planar polarity [Fig. 3(d)]. In either case, our results suggest that the maximum plateau values of structural disorder we observe in both wild-type and *sna twi* embryos reflect biological or physical constraints in the tissue that can be reached via different developmental trajectories.

C. Internal stresses from myosin planar polarity play central roles in generating structural disorder in the germband

As external stresses from the ventral furrow were not sufficient to explain the structural disorder increases in the germband, we wondered if internal stresses associated with actomyosin contractility in the germband might be respon-

sible for structural disorder in the tissue. To explore this possibility, we investigated two different mutants that disrupt AP patterning systems required for myosin planar polarity in the germband. *Krüppel* (*Kr*) mutants have partially disrupted AP patterning and display disrupted myosin planar polarity and reduced cell rearrangement in the central region of the germband [Fig. 4(a)]. In contrast, *bicoid nanos torso-like* (*bcd nos tsl*) mutants have more fully disrupted AP patterning, displaying disrupted myosin planar polarity in the germband as well as disrupted posterior midgut invagination [Fig. 4(b)]. Both mutants are expected to have disrupted internal stresses within the germband, while *bcd nos tsl* is expected to additionally have disrupted external stresses along the AP axis.

Both mutants display low values of Φ_{vol} prior to axis elongation, similar to that in wild-type embryos [Fig. 4(c); see also Figs. S9 and S10 [30]]. Φ_{vol} begins to increase around the same time as in wild-type embryos, just after $t = 0$, and increases at a slower rate, consistent with internal stresses and/or cell rearrangements driving this disorder. Notably, the *bcd nos tsl* mutant does not reach the maximum disorder values observed in wild-type embryos [Fig. 4(c)]. The volumetric disorder reductions [Fig. 4(g)] are associated with strongly reduced cell rearrangements in these embryos [Fig. 4(f)]. These results show that volumetric disorder is strongly linked with AP patterning. The results from *Kr* mutants demonstrate that internal stresses and cell rearrangements associated with myosin planar polarity contribute to volumetric disorder. The stronger effects in *bcd nos tsl* mutants might be explained by more severely disrupted myosin planar polarity and/or disrupted posterior midgut invagination.

To distinguish between these possibilities, we performed our analyses on a previously published movie of a *torso* (*tor*) mutant embryo with a cauterization perturbation [20]. Posterior midgut invagination, but not myosin planar polarity, is disrupted in *tor* mutants, and the cauterization perturbation further reduced external stresses along the AP axis. We found that this embryo displays volumetric disorder similar to in wild-type embryos (Fig. S11 [30]), suggesting that planar polarized myosin is sufficient to promote high levels of volumetric disorder in the germband even in a situation with reduced external stress along the AP axis. Taken together, these results reveal a key role for internal stresses in driving volumetric disorder in the germband.

Both *Kr* and *bcd nos tsl* mutants also display low values of Φ_{shear} prior to axis elongation, similar to wild-type embryos, before beginning to increase around the onset of axis elongation [Fig. 4(c)]. In *Kr* mutants, shear deformations are not evenly distributed across the germband, being more concentrated at the posterior end where midgut invagination is pulling on the germband [Fig. 4(d)]. This effect is less pronounced in wild-type embryos in which cell rearrangements can help relax this stretch. *Kr* mutants reach about the same maximum plateau value of Φ_{shear} as wild-type embryos [Fig. 4(c)], suggesting that internal myosin planar polarity is not essential for generating high levels of shear disorder and that external stresses might play a more dominant role. To explore the role of external stresses further, we examined Φ_{shear} in the *tor* mutant movie with disrupted posterior midgut invagination; Φ_{shear} takes on low to moderate values that do not increase during axis elongation, supporting the idea that external stresses play a key role in reaching high levels of Φ_{shear} (Fig. S11 [30]).

Given the strong stretching observed in the germband of *Kr* mutants, we examined how tissue-level stretching contributes to Φ_{shear} by calculating an alternative shear order parameter in which $\overline{shear_n}$, the mean value of $shear_n$ at each time point, is subtracted from the value of $shear_n$ for each triangle, prior to calculating the order parameter, $\Phi_{\text{shear,alt}} = \langle \ln(|shear_n - \overline{shear_n}|) \rangle$. A stretched hexagonal lattice has $\Phi_{\text{shear,alt}} = 0$. For wild-type and *sna twi* mutant embryos, this alternative approach does not yield significantly different results (Fig. S12 [30]), indicating that variation in the extent of triangle stretching dominates over the average stretching of the whole tissue. In *Kr* mutants and to a lesser extent in *bcd nos tsl* mutants, we see reductions in $\Phi_{\text{shear,alt}}$ compared to Φ_{shear} at later times, indicating that overall tissue stretch has larger contributions to Φ_{shear} in these contexts (Fig. S12 [30]).

In *bcd nos tsl* mutants, Φ_{shear} increases rapidly just prior to the onset of axis elongation before plateauing early at a reduced level of shear disorder [Fig. 4(c)]. Given the disruption of myosin planar polarity and posterior midgut invagination in these embryos, these results support the idea that this early increase in shear disorder is driven by the ventral furrow and then maintained throughout the rest of axis elongation. Interestingly, *bcd nos tsl* mutants appear to be more rapidly stretched by the ventral furrow compared to wild-type embryos, with a faster shear disorder increase [Figs. 4(c), 4(e) and 4(h)], suggesting that the germband may be more compliant in *bcd nos tsl* mutants.

Taken together, these results demonstrate central roles for internal stresses associated with myosin planar polarity in tissue structural disorder. The effects of internal stresses and cell intercalation are most clear in the signatures of Φ_{vol}, although other factors also contribute. In addition, both internal stresses associated with myosin planar polarity and external stresses associated with posterior midgut invagination and ventral furrow invagination contribute to Φ_{shear} in the germband.

D. Linking structural disorder to tissue elongation

To combine and visualize all of our data on structural disorder, we plotted the trajectories that wild-type and mutant embryos take in the Φ_{vol} and Φ_{shear} parameter space during axis elongation. We find that each embryo group takes a distinct path through the parameter space as volumetric and shear disorder grow. However, all trajectories appear to converge towards and not exceed the values of $\Phi_{\text{vol}} \approx 0.20$ and $\Phi_{\text{shear}} \approx -1.5$ [Fig. 5(a)], which correspond to the plateau values in wild type. It was unclear why volumetric and shear disorder plateau and what sets these plateau values.

One possibility is that tissue elongation requires a concomitant increase in disorder. In this case, structural disorder is essentially a readout of the history of tissue remodeling via cell rearrangements and/or cell stretching. However, this is not consistent with the observation that both Φ_{vol} and Φ_{shear} plateau at $t = 5$–10 min in wild-type embryos, well before the tissue has fully elongated [Fig. 5(b) and Fig. S13 [30]].

A second possibility is that structural disorder is instead a readout of the current rate of tissue remodeling. In this case, structural disorder should be directly related to the instanta-

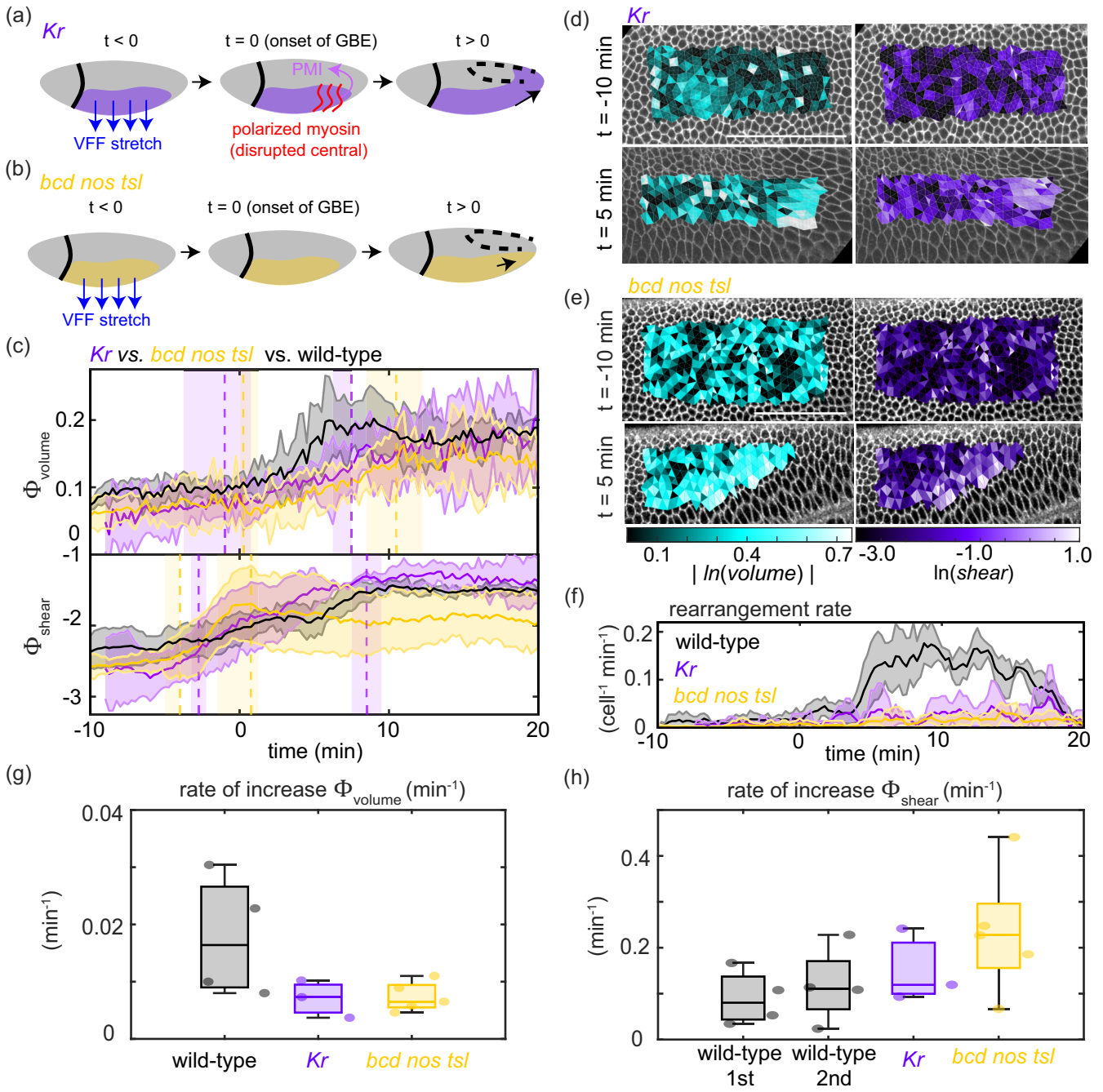

FIG. 4. Structural disorder growth is disrupted in mutant embryos with disrupted AP patterning. (a) Schematics of key developmental events in *Kr* mutant embryos with disrupted myosin planar polarity in anterior and central regions of the germband. Disrupting myosin planar polarity alters the anisotropic internal stress patterns in the germband. (b) Schematics of key developmental events in *bcd nos tsl* mutant embryos with disrupted myosin planar polarity in the germband and disrupted posterior midgut invagination. Disrupting posterior midgut invagination alters the external stress patterns acting on the germband. (c) Average Φ_{vol} and Φ_{shear} in the germband of *Kr* (purple) ($N = 3$) and *bcd nos tsl* (yellow) ($N = 5$) mutants compared to wild type (black). Shaded error bars represent standard deviation between embryos. Vertical dashed lines indicate locations of slope changes within each embryo group. (d) Volumetric (cyan) and shear (purple) deformation for the tissue triangulation at $t = -10$ and 5 min in *Kr* mutants. (e) Volumetric (cyan) and shear (purple) deformation for the tissue triangulation in *bcd nos tsl* mutant embryos at $t = -10$ and 5 min. (f) Cell rearrangement rates in *Kr*, *bcd nos tsl*, and wild-type embryos. Rates of volumetric (g) and shear (h) disorder growth [average slope of $\Phi_{shear}(t)$ between slope changes] for wild-type, *Kr*, and *bcd nos tsl* embryos. Wild-type 1st and wild-type 2nd correspond to the first and second shear disorder increases in Fig. 2(a).

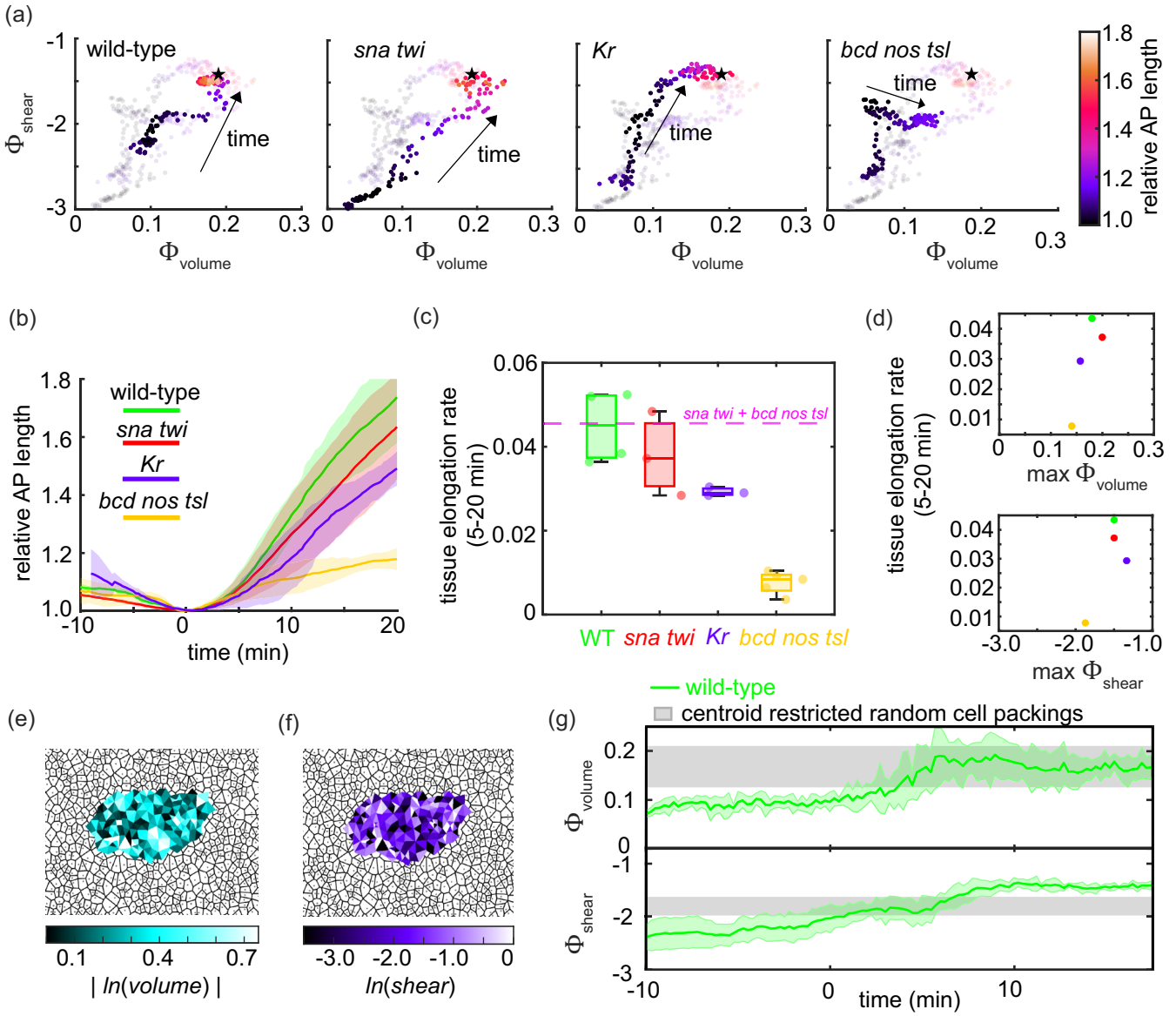

FIG. 5. Linking volumetric and shear disorder patterns to tissue elongation. (a) Trajectories through the $\Phi_{shear} - \Phi_{vol}$ parameter space over time during axis elongation. The extent of tissue elongation is indicated by the color of each data point. Stars, point toward which volumetric and shear disorder converge. (b) Tissue elongation over time for wild type (green), *sna twi* (red), *Kr* (purple), and *bcd nos tsl* (yellow). Mean ± standard deviation between embryos. The procedure for analyzing tissue length is provided in the Methods section. (c) Average tissue elongation rates between $t = 5$ and 20 min for each group. The sum of elongation rates for *sna twi* and *bcd nos tsl* embryos is represented by the dashed magenta line. (d) Tissue elongation rate vs plateau values of Φ_{vol} and Φ_{shear}. (e), (f) Randomly generated tilings of cell packings using densities and minimum spacings characteristic of the germband. Overlaid volumetric and shear deformations for the resulting triangulation. (g) The plateau value of Φ_{vol} in the wild-type germband (green) overlaps the range of values for random cell packings with densities and minimum spacings characteristic of the germband (gray horizontal band). The small, intermediate plateau of Φ_{shear} in the germband (green) overlaps with the range of values for random cell packings with densities and minimum spacings characteristic of the germband (gray horizontal band). The final plateau exceeds values for random packings, likely due to anisotropy in the germband.

neous rates of tissue elongation or cell rearrangement. The maximum value of disorder would then be set by embryonic mechanics that control tissue deformation rates. Supporting this idea, we found that Φ_{vol} reaches a maximum at the same time that the maximum rate of cell rearrangement is achieved in wild-type embryos at $t = 5$ min [cf. Figs. 2(a) and 2(f)]. However, after this time point, Φ_{vol} maintains its plateau value, while the cell rearrangement rate slowly decreases [cf. Figs. 2(a) and 2(f)]. Moreover, the average tissue elongation rates from $t = 5$–20 min for wild type, *sna twi*, and *Kr* take on different values, while Φ_{vol} and Φ_{shear} have similar plateau values [Figs. 5(c) and 5(d)]. Thus, disorder is not simply related with either the extent or the instantaneous rate of tissue remodeling.

A third possibility is that the observed disorder plateaus might reflect some type of geometrical [31] or maximum entropy constraint [32]. In this case, disorder might increase due to tissue remodeling but then reach a maximum value

set by limits on tissue disorder, even as the tissue continues remodeling. To explore this possibility, we needed a reference for comparing the magnitudes of Φ_{vol} and Φ_{shear} observed in the germband. We started by comparing our results to model tissues with random cell packings. We generated tilings of random cell packings using ranges of cell densities and minimum centroid spacings that we measured in the germband movies (Materials and Methods) [Figs. 5(e) and 5(f) and Fig. S14 [30]] and quantified the range of values of Φ_{vol} and Φ_{shear} for the resulting packings [Fig. 5(g) and Fig. S14 [30]].

Notably, the maximum plateau value of Φ_{vol} for the wild-type germband falls within the range we calculated for random packings with minimum cell centroid spacings characteristic of the germband [Fig. 5(g)]. Without restricting centroid spacing, a purely random cell packings had disorder values well above those in the germband [Fig. S14(b) [30]]. This indicates that, in terms of density fluctuations, cell packings in the germband are initially more ordered than random cell packings and become more disordered as the tissue remodels, up until having features similar to those of a random packing. This suggests that random packings with a minimum cell centroid spacing may represent a limit on tissue disorder in this context.

In contrast, Φ_{shear} in the germband reaches larger values than calculated for random cell packings [Fig. 5(g)]. This is consistent with tissue-level cell stretching in the germband that can produce higher shear deformations than expected for random, isotropic packings. Interestingly, the values of Φ_{shear} for random packings do match the small, intermediate plateau we observe in wild-type embryos, during a period when cells in the tissue are reorienting [Fig. 5(g)]. In addition, the values of Φ_{shear} in *tor* mutant embryos, which have disrupted posterior midgut invagination but normal myosin planar polarity, overlap the range of values for random packings (Fig. S11 [30]). This suggests that random packings may also represent a limit on shear disorder in relatively isotropic tissues, and that tissue-level anisotropy from external or internal stresses can modulate this.

Finally, we asked how volumetric and shear disorder patterns are ultimately linked with the axis elongation process. Although tissue elongation rates were not simply related to either Φ_{vol} or Φ_{shear} [Fig. 5(d)], we noted that the embryos that elongated the most (wild type, *sna twi*, *Kr*) had relatively high Φ_{vol} and/or Φ_{shear}, while the embryos that elongated significantly less (*bcd nos tsl*) had reduced values of both Φ_{vol} and Φ_{shear} [Figs. 5(a)–5(c)]. This suggests a combination of volumetric disorder and shear disorder are central to tissue remodeling. Intriguingly, the sum of tissue elongation rates for *sna twi* (with disrupted ventral furrow) and *bcd nos tsl* (with disrupted myosin planar polarity and posterior midgut invagination) is nearly identical to the tissue elongation rate for wild type [Fig. 5(c)]. This suggests that internal stresses associated with myosin planar polarity, external stresses from posterior midgut invagination, and external stresses from ventral furrow invagination may contribute in an additive fashion to axis elongation, although they are not additive in disorder. Taken together, these results demonstrate that rapid tissue elongation is linked with strong patterns of growing volumetric and shear disorder and suggest that there are physical limits on tissue disorder in this context.

III. DISCUSSION

Here we showed that volumetric and shear structural disorder increase in the germband epithelium during body axis elongation in *Drosophila*. We find characteristic signatures of disorder that are shared among wild-type embryos and are correlated with developmental events involving changing patterns of internal and/or external stresses acting on the germband. By studying mutant embryos with altered patterns of internal and external stresses, we show that internal stress patterns associated with myosin planar polarity and cell rearrangement are strongly linked with signatures in Φ_{vol} and also contribute to Φ_{shear}, while external stress patterns associated with ventral furrow and posterior midgut invagination have large contributions to Φ_{shear}. Although the structural disorder metrics begin to increase around the onset of axis elongation, they both quickly plateau at values that are then maintained. These plateau values are similar to those for random cell packings, suggesting this may reflect a limit on tissue behavior. Finally, we find that high volumetric and shear disorder is linked with rapid tissue elongation, although the precise balance between volumetric and shear disorder is distinct in the germband of wild-type and mutant embryos that elongate significantly.

We report links between cell intercalations driven by internal stresses and both Φ_{vol} and Φ_{shear}. Around a quartet of cells involved in a single cell rearrangement, there are volumetric and shear deformations as cells change shape in order to form a vertex where four or more cells meet (Fig. S15 [30]). When averaged across the tissue, these intercalation-associated deformations contribute to the increases in structural disorder over time. Notably, these effects are distinguishable in the delays or reductions of volumetric disorder in *Kr* and *bcd nos tsl* but not *tor* mutant embryos. In addition, external stresses associated with VFF and PMI contribute to structural disorder, with the effects most clearly distinguishable in the reductions of Φ_{shear} in *sna twi*, *bcd nos tsl*, and *tor* mutant embryos.

Our findings demonstrate that structural disorder grows during germband extension and is an important feature of this remodeling tissue. This extends prior work on topological disorder, which showed that the germband initially contains cells that are predominantly hexagonal in shape prior to axis elongation, before topological disorder increases during axis elongation [4]. In contrast, in the developing *Drosophila* wings and notum, cell rearrangements and junction fluctuations can increase geometric order, converting initially disordered cell packings into more hexagonally packed cells [33,34]. In proliferating epithelia, cell divisions can also contribute to topological disorder during development [35]. Our results add to a growing body of work implicating geometric or structural signatures in jamming transitions, cell migration, wound healing, development, and cancer metastasis [13,24–29,31,36–40]. We find that the initial growth of structural disorder in the germband is correlated with the onset of rapid cell rearrangements and tissue remodeling, consistent with a possible solidlike-fluidlike transition [13]. However, the following nearly steplike disorder increases appear more like signatures of structural changes associated with specific developmental events.

It remains unclear if structural disorder is primarily an indicator of tissue remodeling or instead also feeds back to influence tissue remodeling. In particular, it is not known if the current structural order (disorder) in a tissue might facilitate (hinder) cell rearrangement and tissue remodeling. We find that after the germband reaches a maximum plateau value of volumetric disorder in wild-type and *sna twi* embryos, the cell rearrangement rates slowly begin to decrease. This suggests that cell rearrangement promotes disorder and that this disorder then might hinder further rearrangement. This is consistent with ideas from recent findings that disordered packings of cells extend more slowly than more ordered packings in some contexts [41,42]. Future studies will be needed to fully address how tissue disorder impacts tissue remodeling and flow.

Our findings suggest that there are limits on the maximum structural disorder in the germband. The maximum volumetric disorder observed in the germband of wild-type and mutant embryos matches that of random tilings of cells with densities and minimum cell centroid spacings characteristic of the germband. In this study, we have compared germband cell packings to random tilings based on Voronoi tessellations and random sequential addition of seeds, but we note that there are many procedures for generating random tilings that could be explored in future work. In our random cell packings, volumetric disorder is strongly influenced by the minimum spacing between cell centroids (Fig. S14 [30]), suggesting that a minimum spacing between cells might underlie the limits on structural disorder we observe in the germband. This minimum spacing might arise because the apical domain is tightly regulated and maintained by epithelial cells or because nuclei might influence cell packings. Consistent with this possibility, recent reports highlight the importance of nucleus size and packings [43,44].

Our findings support the notion that internal stresses from myosin planar polarity and external stresses from ventral furrow and posterior midgut invagination all contribute to tissue remodeling. There have been conflicting reports on the role of the ventral furrow in germband extension. It has recently been proposed that the stretch from ventral furrow invagination recruits myosin to cell junctions in the germband in a planar polarized fashion via mechanical feedback mechanisms, which then promote tissue flow [18]. However, other studies have shown that myosin planar polarity acts downstream of AP patterning systems [6,7,21] and that the germband displays cell rearrangements and tissue elongation even when the ventral furrow is disrupted [10,13,45,46]. Here, we find delays in disorder, cell rearrangement, and tissue elongation in *sna twi* mutant embryos, suggesting that the ventral furrow facilitates but is not required for tissue remodeling.

Taken together, our results identify growing structural disorder as a key feature of tissue remodeling. It remains unclear how structural disorder impacts tissue mechanics and might in turn influence patterns of cell rearrangements and tissue elongation during morphogenetic events. Moreover, it is not known how spatiotemporal patterns of cellular contractile and adhesive machineries drive structural disorder and might be influenced by tissue structure through mechanosensitive mechanisms. Future work will be needed to clarify these questions and explore how tissue disorder ultimately impacts tissue behavior and function.

IV. MATERIALS AND METHODS

A. Fly lines and genetics

Fly stocks were from the Bloomington *Drosophila* Stock Center (BDSC) unless otherwise noted. Wild-type control embryos were *yw* with one maternal copy of an sqh-gap43:mCherry transgene [47] to label cell membranes and two maternal copies of sqh-GFP:ZipWT to label myosin II [48] (not used in this study). The *Krüppel* (*Kr*) mutant fly stock was a gift from Eric Wieschaus [6]. *Kr* embryos were zygotic Kr^{1} mutants with a sqh-gap43:mCherry transgene. The movies of *snail twist* (*sna twi*) and *bicoid nanos torso-like* (*bcd nos tsl*) mutant embryos were from Wang *et al.* [13]. *sna twi* embryos were zygotic sna^{IIG05} twi^{DfS60} mutants and expressed Spider:GFP to visualize cell outlines. The *bcd nos tsl* maternal mutant embryos were the progeny of bcd^{E1} nos^{L7} tsl^{146} homozygous females and expressed Resille:GFP to visualize cell outlines. The movie of the *torso* (*tor*) mutant embryo with cauterization was from supplementary video 11 in [20]. The *tor* maternal mutant embryos were progeny of tor^{4} homozygous females and expressed Ecad:GFP to visualize cell outlines.

B. Embryo preparation

Embryos were generated at 23 °C. Embryos were collected at stage 6, dechorionated in 50% bleach for 2 min, washed with water for 2 min, and mounted on a custom-made imaging chamber in a 50:50 mixture of halocarbon oils 27 and 700 between an oxygen-permeable membrane (YSI Incorporated) and a glass coverslip. Embryos are gently pushed against the coverslip so that a small fraction of the embryo is flat against the coverslip. The images shown are projections of z-slices several microns from the coverslip at the level of adherens junctions.

C. Confocal time-lapse imaging

Imaging was performed at room temperature (approximately 18 ± 1 °C) on a Zeiss LSM 880 laser-scanning confocal microscope. Embryos were placed in a ventrolateral or ventral orientation for imaging. A 561 nm diode laser was used for imaging mCherry, and a 488 nm argon laser excitation was used for GFP. Imaging was performed using the Airyscan FAST module and a C-Apo 40X/1.2 NA water-immersion objective (Carl Zeiss, Germany). Movies were acquired as 9.1 μm z-stacks with a 0.7 μm z-step every 15 s. The first image was captured at the most apical surface of the embryo. Movies were rotated and z-projections taken using the Fiji distribution of ImageJ [49,50]. Each z-projection was performed by taking a maximum intensity projection of three consecutive z-slices at the apical junctional plane of the tissue.

Separate movies were captured for imaging the germband and ventral furrow regions of the embryo. Embryos for germband movies were oriented ventrolaterally, and embryos for ventral furrow movies were oriented ventrally. Regions of interests for each movie were defined, and cells were segmented based on cell membrane markers. For movies of the germband, the confocal imaging field of view is chosen so that the cephalic furrow is just visible at one edge and the ventral furrow is just visible at another edge of the field during time

periods of the movies. Our analysis ROI is defined as follows: two to three cells away from the cephalic furrow at the anterior side of the ROI, two to three cells away from the ventral furrow at the ventral side of the ROI, the boundary between the germband and amnioserosa or the imaging field of view at the dorsal side of the ROI, and the boundary of the imaging field of view on the posterior side of the ROI. Our results are not significantly affected by increasing or decreasing the size of the ROI (Figs. S2 and S3 [30]), and they are similar to results obtained by applying our analyses to previously published images from *in toto* microscopy of embryos mounted in agarose [51] (Fig. S4 [30]). For the ventral furrow movies, analysis concludes prior to tissue invagination and focuses on in-plane stretching.

D. Cell segmentation analysis

Cell outlines were identified using a custom MATLAB code that implements a watershed algorithm [52] combined with a mask. The segmentation output was imported into the SEGGA tissue segmentation and analysis software [45] using a custom MATLAB script, and manual corrections were performed using the SEGGA GUI. In the final segmentation, each cell is represented as a polygon with straight edges. Custom MATLAB scripts were used to further process and analyze data.

E. Tissue elongation

For all measurements of germband tissue length, the same ROI used for analyzing disorder was used for analyzing tissue length. Briefly, all cells that stay within the ROI for the whole movie are identified and tracked. Changes in the length of this group of cells along the AP (horizontal) axis over time are reported, relative to the length at $t = 0$.

F. Aligning movies

To compare movies, $t = 0$ min was taken as the onset of germband extension, which was identified by finding the time point corresponding to the minimum germband tissue length, when considering the group of cells that were in the ROI at all time frames. In addition, manual inspection confirmed that the cephalic furrow formation process is well-aligned by this definition of $t = 0$ in each movie.

G. Rearrangement rate analysis

Cells within the ROI were tracked and cell rearrangement events identified using SEGGA [45]. The number of rearrangements per cell in each time frame was calculated by dividing the number of cell neighbors lost in each time frame by the number of cells analyzed in that frame.

H. Calculation of Φ_{vol} and Φ_{shear} and identifying changes in slope in these disorder metrics

The tissue was triangulated by finding the centers of all cells in the ROI and connecting adjacent centers. If four or more segments from a grouping of cells meet at a single node, an additional node was added at this point to create the triangulation [53]. Using this triangulation, Φ_{vol} and Φ_{shear} were calculated as shown previously [29]. Briefly, the volumetric and shear order parameters are defined as $\Phi_{vol} = \langle[\ln(vol_n)]^2\rangle$ and $\Phi_{shear} = \langle\ln(shear_n)\rangle$. The volumetric and shear deformations for individual triangles are calculated from the deformation gradient, $\boldsymbol{F}$, where $vol_n = det(\boldsymbol{F})$ and $shear_n = [tr(\boldsymbol{F}^T\boldsymbol{F})/det(\boldsymbol{F})] - 2$. The deformation gradient is defined by the current and reference configurations $\boldsymbol{F} = \boldsymbol{T}_n\boldsymbol{T}_r^{-1}$. The current configuration for each triangle, n, is defined by the three vertices that link adjacent cells and is $\boldsymbol{T}_n = \begin{bmatrix} x_{n1} - x_{n0} & x_{n2} - x_{n0} \\ y_{n1} - y_{n0} & y_{n2} - y_{n0} \end{bmatrix}$. The reference configuration is defined by an equilateral triangle with an area, A, equal to the average value for the time frame and is $\boldsymbol{T}_r = \sqrt{A}\begin{bmatrix} 1 & 1/2 \\ 0 & \sqrt{(3)}/2) \end{bmatrix}$. Time points of changes in slope in $\Phi_{vol}(t)$ and $\Phi_{shear}(t)$ were identified by first visually identifying the number of slope changes (n) and then using a custom MATLAB script to fit $(n + 1)$ linear fits to the volumetric and shear order parameter curves. This process was repeated for every iteration of possible time intervals until the sum of the residuals for all $(n + 1)$ linear fits were minimized. Error bars for the timing of these slope changes correspond to where the root-mean-squared deviation was within 10%.

I. Random cell tiling simulation

We generated randomly organized cell packings and calculated Φ_{vol} and Φ_{shear} for these random packings. To do this, we seeded points within a known area to act as the nucleation centers, i.e., random sequential addition (RSA). The number of nucleation points was varied to match the range of cell densities observed in germband movies. Additionally, we performed this analysis with and without varying the minimum distance between nucleation points to match the minimum spacing of cell centers observed in germband movies of 3–4 μm; this may help to account for biological mechanisms that maintain cell size and shape and/or incompressibility of cell nuclei or other internal cellular structures. We generated five unique Voronoi tilings and moved the seed points to the center of mass for each Voronoi cell (centroidal Voronoi diagram algorithm) [54]. We did this for each set of parameters and analyzed five different ROIs for each image. Each image was processed with the same pipeline as the germband movies. Briefly, the images were segmented with our algorithm and manually corrected in SEGGA before calculating Φ_{vol} and Φ_{shear}.

Data plotted represent mean value ± standard deviation unless otherwise noted.

The data in this paper are available from the corresponding author upon reasonable request.

Custom MATLAB scripts are available from the corresponding author upon reasonable request.

ACKNOWLEDGMENTS

We thank Erika Kusaka for help generating fly stocks, Rob Campbell for the MATLAB function shadederrorbar, and members of the Kasza Lab, Andrew Cupo, Haiqian Yang,

Ming Guo, and Max Bi for helpful discussions. This work was supported by the National Institute of General Medical Sciences of the National Institutes of Health Award No. R35GM138380 to K.E.K. and Eunice Kennedy Shriver National Institute of Child Health & Development of the National Institutes of Health Grant No. F31HD105405 to C.C. The content is solely the responsibility of the authors and does not necessarily represent the official views of the National Institute of Health. K.E.K. holds an NSF CAREER Award, Packard Fellowship, and Sloan Research Fellowship in Physics.

C.C. and K.E.K. initiated the project, designed the experiments, and developed the project. C.C performed all experiments. C.C. and C.A. developed the code for image processing and data analysis. C.C. and V.A. created the plots, images, and graphics for the figures. C.C. and K.E.K. wrote the manuscript. All authors contributed to data interpretation and approved the final manuscript.

[1] T. Lecuit and P.-F. Lenne, Cell surface mechanics and the control of cell shape, tissue patterns and morphogenesis, Nat. Rev. Mol. Cell Biol. **8**, 633 (2007).

[2] F. Jülicher and S. Eaton, Emergence of tissue shape changes from collective cell behaviours, Semin. Cell Dev. Biol. **67**, 103 (2017).

[3] R. M. Herrera-Perez and K. E. Kasza, Biophysical control of the cell rearrangements and cell shape changes that build epithelial tissues, Curr. Opin. Gen. Dev. **51**, 88 (2018).

[4] J. A. Zallen and R. Zallen, Cell-pattern disordering during convergent extension in *Drosophila*, J. Phys.: Condens. Matter **16**, S5073 (2004).

[5] T. C. Hales, The honeycomb conjecture, Discrete Comput. Geom. **25**, 1 (2001).

[6] K. D. Irvine and E. Wieschaus, Cell intercalation during *Drosophila* germband extension and its regulation by pair-rule segmentation genes, Development **120**, 827 (1994).

[7] J. A. Zallen and E. Wieschaus, Patterned gene expression directs bipolar planar polarity in *Drosophila*, Develop. Cell **6**, 343 (2004).

[8] C. Bertet, L. Sulak, and T. Lecuit, Myosin-dependent junction remodelling controls planar cell intercalation and axis elongation, Nature (London) **429**, 667 (2004).

[9] R. Fernandez-Gonzalez, S. d. M. Simoes, J.-C. Röper, S. Eaton, and J. A. Zallen, Myosin II dynamics are regulated by tension in intercalating cells, Develop. Cell **17**, 736 (2009).

[10] C. M. Lye, G. B. Blanchard, H. W. Naylor, L. Muresan, J. Huisken, R. J. Adams, and B. Sanson, Mechanical coupling between endoderm invagination and axis extension in *Drosophila*, PLOS Biol. **13**, e1002292 (2015).

[11] M. Dicko, P. Saramito, G. B. Blanchard, C. M. Lye, B. Sanson, and J. Étienne, Geometry can provide long-range mechanical guidance for embryogenesis, PLoS Comput. Biol. **13**, e1005443 (2017).

[12] S. J. Streichan, M. F. Lefebvre, N. Noll, E. F. Wieschaus, and B. I. Shraiman, Global morphogenetic flow is accurately predicted by the spatial distribution of myosin motors, eLife **7**, e27454 (2018).

[13] X. Wang, M. Merkel, L. B. Sutter, G. Erdemci-Tandogan, M. L. Manning, and K. E. Kasza, Anisotropy links cell shapes to tissue flow during convergent extension, Proc. Natl. Acad. Sci. USA **117**, 13541 (2020).

[14] M. Rauzi, P. Verant, T. Lecuit, and P.-F. Lenne, Nature and anisotropy of cortical forces orienting *Drosophila* tissue morphogenesis, Nat. Cell Biol. **10**, 1401 (2008).

[15] L. C. Butler, G. B. Blanchard, A. J. Kabla, N. J. Lawrence, D. P. Welchman, L. Mahadevan, R. J. Adams, and B. Sanson, Cell shape changes indicate a role for extrinsic tensile forces in *Drosophila* germ-band extension, Nat. Cell Biol. **11**, 859 (2009).

[16] M. Rauzi, U. Krzic, T. E. Saunders, M. Krajnc, P. Ziherl, L. Hufnagel, and M. Leptin, Embryo-scale tissue mechanics during *Drosophila* gastrulation movements, Nat. Commun. **6**, 8677 (2015).

[17] J. C. Yu and R. Fernandez-Gonzalez, Local mechanical forces promote polarized junctional assembly and axis elongation in *Drosophila*, eLife **5**, e10757 (2016).

[18] H. J. Gustafson, N. Claussen, S. De Renzis, and S. J. Streichan, Patterned mechanical feedback establishes a global myosin gradient, Nat. Commun. **13**, 7050 (2022).

[19] J. T. Blankenship, S. T. Backovic, J. Sanny, O. Weitz, and J. A. Zallen, Multicellular rosette formation links planar cell polarity to tissue morphogenesis, Develop. Cell **11**, 459 (2006).

[20] C. Collinet, M. Rauzi, P.-F. Lenne, and T. Lecuit, Local and tissue-scale forces drive oriented junction growth during tissue extension, Nat. Cell Biol. **17**, 1247 (2015).

[21] A. C. Paré, A. Vichas, C. T. Fincher, Z. Mirman, D. L. Farrell, A. Mainieri, and J. A. Zallen, A positional Toll receptor code directs convergent extension in *Drosophila*, Nature (London) **515**, 523 (2014).

[22] M. Leptin, *Drosophila* gastrulation: From pattern formation to morphogenesis, Annu. Rev. Cell Dev. Biol. **11**, 189 (1995).

[23] D. Kong, F. Wolf, and J. Großhans, Forces directing germ-band extension in *Drosophila* embryos, Mech. Dev. **144**, 11 (2017).

[24] D. Bi, J. H. Lopez, J. M. Schwarz, and M. Lisa Manning, Energy barriers and cell migration in densely packed tissues, Soft Matter **10**, 1885 (2014).

[25] J.-A. Park, J. H. Kim, D. Bi, J. A. Mitchel, N. T. Qazvini, K. Tantisira, C. Y. Park, M. McGill, S.-H. Kim, B. Gweon, J. Notbohm, R. Steward Jr., S. Burger, S. H. Randell, A. T. Kho, D. T. Tambe, C. Hardin, S. A. Shore, E. Israel, D. A. Weitz, D. J. Tschumperlin, E. Henske, S. T. Weiss, M. L. Manning, J. P. Butler, J. M. Drazen, and J. J. Fredberg, Unjamming and cell shape in the asthmatic airway epithelium, Nat. Mater. **14**, 1040 (2015).

[26] D. Bi, J. H. Lopez, J. M. Schwarz, and M. L. Manning, A density-independent rigidity transition in biological tissues, Nat. Phys. **11**, 1074 (2015).

[27] D. Bi, X. Yang, M. C. Marchetti, and M. L. Manning, Motility-driven glass and jamming transitions in biological tissues, Phys. Rev. X **6**, 021011 (2016).

[28] A. Jain, V. Ulman, A. Mukherjee, M. Prakash, M. B. Cuenca, L. G. Pimpale, S. Münster, R. Haase, K. A. Panfilio, F. Jug, S. W. Grill, P. Tomancak, and A. Pavlopoulos, Regionalized

tissue fluidization is required for epithelial gap closure during insect gastrulation, Nat. Commun. **11**, 5604 (2020).

[29] H. Yang, A. F. Pegoraro, Y. Han, W. Tang, R. Abeyaratne, D. Bi, and M. Guo, Configurational fingerprints of multicellular living systems, Proc. Natl. Acad. Sci. USA **118**, e2109168118 (2021).

[30] See Supplemental Material at http://link.aps.org/supplemental/10.1103/PRXLife.2.043004 for fifteen additional supplemental figures and captions.

[31] L. Atia, D. Bi, Y. Sharma, J. A. Mitchel, B. Gweon, S. A Koehler, S. J. DeCamp, B. Lan, J. H. Kim, and R. Hirsch, Geometric constraints during epithelial jamming, Nat. Phys. **14**, 613 (2018).

[32] T. C. Day, S. S. Höhn, S. A. Zamani-Dahaj, D. Yanni, A. Burnetti, J. Pentz, A. R. Honerkamp-Smith, H. Wioland, H. R. Sleath, W. C. Ratcliff, R. E. Goldstein, and P. J. Yunker, Cellular organization in lab-evolved and extant multicellular species obeys a maximum entropy law, eLife **11**, e72707 (2022).

[33] A.-K. Classen, K. I. Anderson, E. Marois, and S. Eaton, Hexagonal packing of *Drosophila* wing epithelial cells by the planar cell polarity pathway, Develop. Cell **9**, 805 (2005).

[34] S. Curran, C. Strandkvist, J. Bathmann, M. De Gennes, A. Kabla, G. Salbreux, and B. Baum, Myosin II controls junction fluctuations to guide epithelial tissue ordering, Develop. Cell **43**, 480 (2017).

[35] M. C. Gibson, A. B. Patel, R. Nagpal, and N. Perrimon, The emergence of geometric order in proliferating metazoan epithelia, Nature (London) **442**, 1038 (2006).

[36] R. Farhadifar, J.-C. Röper, B. Aigouy, S. Eaton, and F. Jülicher, The influence of cell mechanics, cell-cell interactions, and proliferation on epithelial packing, Curr. Biol. **17**, 2095 (2007).

[37] N. Founounou, R. Farhadifar, G. M. Collu, U. Weber, M. J. Shelley, and M. Mlodzik, Tissue fluidity mediated by adherens junction dynamics promotes planar cell polarity-driven ommatidial rotation, Nat. Commun. **12**, 6974 (2021).

[38] J. H. Kim, A. F. Pegoraro, A. Das, S. A. Koehler, S. A. Ujwary, B. Lan, J. A. Mitchel, L. Atia, S. He, K. Wang, D. Bi, M. H. Zaman, J.-A. Park, J. P. Butler, K. H. Lee, J. R. Starr, and J. J. Fredberg, Unjamming and collective migration in MCF10A breast cancer cell lines, Biochem. Biophys. Res. Commun. **521**, 706 (2020).

[39] N. I. Petridou, B. Corominas-Murtra, C.-P. Heisenberg, and E. Hannezo, Rigidity percolation uncovers a structural basis for embryonic tissue phase transitions, Cell **184**, 1914 (2021).

[40] W. Kang, J. Ferruzzi, C.-P. Spatarelu, Y. L. Han, Y. Sharma, S. A. Koehler, J. A. Mitchel, A. Khan, J. P. Butler, D. Roblyer, M. H. Zaman, J.-A. Park, M. Guo, Z. Chen, A. F. Pegoraro, and J. J. Fredberg, A novel jamming phase diagram links tumor invasion to non-equilibrium phase separation, iScience **24**, 103252 (2021).

[41] F. Brauns, N. H. Claussen, M. F Lefebvre, E. F. Wieschaus, and B. I. Shraiman, The geometric basis of epithelial convergent extension, eLife **13**, RP95521 (2024).

[42] N. H. Claussen, F. Brauns, and B. I. Shraiman, A geometric-tension-dynamics model of epithelial convergent extension, Proc. Natl. Acad. Sci. USA **121**, e2321928121 (2024).

[43] S. Dutta, N. J.-V. Djabrayan, S. Torquato, S. Y. Shvartsman, and M. Krajnc, Self-similar dynamics of nuclear packing in the early *Drosophila* embryo, Biophys. J. **117**, 743 (2019).

[44] S. Kim, R. Amini, S.-T. Yen, P. Pospíšil, A. Boutillon, I. A. Deniz, and O. Campàs, A nuclear jamming transition in vertebrate organogenesis, Nat. Mater. (2024), doi: 10.1038/s41563-024-01972-3.

[45] D. L. Farrell, O. Weitz, M. O. Magnasco, and J. A. Zallen, SEGGA: A toolset for rapid automated analysis of epithelial cell polarity and dynamics, Development **144**, 1725 (2017).

[46] C. M. Lye, G. B. Blanchard, J. Evans, A. Nestor-Bergmann, and B. Sanson, Polarised cell intercalation during *Drosophila* axis extension is robust to an orthogonal pull by invaginating mesoderm, PLoS Biol. **22**, e3002611 (2024).

[47] A. C. Martin, M. Gelbart, R. Fernandez-Gonzalez, M. Kaschube, and E. F. Wieschaus, Integration of contractile forces during tissue invagination, J. Cell Biol. **188**, 735 (2010).

[48] K. E. Kasza, S. Supriyatno, and J. A. Zallen, Cellular defects resulting from disease-related myosin II mutations in *Drosophila*, Proc. Natl. Acad. Sci. USA **116**, 22205 (2019).

[49] C. T. Rueden, J. Schindelin, M. C. Hiner, B. E. DeZonia, A. E. Walter, E. T. Arena, and K. W. Eliceiri, ImageJ2: ImageJ for the next generation of scientific image data, BMC Bioinf. **18**, 529 (2017).

[50] J. Schindelin, I. Arganda-Carreras, E. Frise, V. Kaynig, M. Longair, T. Pietzsch, S. Preibisch, C. Rueden, S. Saalfeld, B. Schmid, J.-Y. Tinevez, D. J. White, V. Hartenstein, K. Eliceiri, P. Tomancak, and A. Cardona, Fiji: an open-source platform for biological-image analysis, Nat. Methods **9**, 676 (2012).

[51] T. Stern, S. Y. Shvartsman, and E. F. Wieschaus, Deconstructing gastrulation at single-cell resolution, Curr. Biol. **32**, 1861 (2022).

[52] L. Vincent and P. Soille, Watersheds in digital spaces: An efficient algorithm based on immersion simulations, IEEE Trans. Pattern Anal. Machine Intell. **13**, 583 (1991).

[53] M. Merkel, R. Etournay, M. Popović, G. Salbreux, S. Eaton, and F. Jülicher, Triangles bridge the scales: Quantifying cellular contributions to tissue deformation, Phys. Rev. E **95**, 032401 (2017).

[54] M. A. Klatt, J. Lovrić, D. Chen, S. C. Kapfer, F. M. Schaller, P. W. A. Schönhöfer, B. S. Gardiner, A.-S. Smith, G. E. Schröder-Turk, and S. Torquato, Universal hidden order in amorphous cellular geometries, Nat. Commun. **10**, 811 (2019).